Original Article

Investigation of the Corrosion Resistance Mechanism of Stellite 6 Coating on AISI 1045 Steel Fabricated by Laser Cladding Technology

Phan Truong Duy[1], Thang Le Toan[2,3]*, Nguyen Van Cuong[2], Huynh Chi Linh[1]

[1]Faculty of Mechanical Engineering, Vinh Long University of Technology Education (VLUTE), Vinh Long Province, Vietnam.
[2]Faculty of Mechanical Engineering, University of Transport and Communications (UTC), Hanoi, Vietnam.
[3]National Research Institute of Mechanical Engineering, Hanoi, Vietnam.

*Corresponding Author : thanglt@utc.edu.vn

Abstract - The study investigates the corrosion resistance mechanism of a Stellite 6 coating deposited on AISI 1045 steel by using laser cladding technology. The objective was to clarify the microstructural characteristics, electrochemical behavior, and protective mechanism of the coating. The Stellite 6 alloy, composed mainly of cobalt, chromium, tungsten, and carbon, was deposited using a 2 kW Yb fiber laser under optimized parameters to form a dense, defect-free coating metallurgically bonded to the substrate. Microstructural and Compositional analyses by optical microscopy and SEM–EDS revealed a fine columnar dendritic structure with minimal dilution and a Cr and Co-rich surface layer containing carbide phases such as Cr_7C_3 and Co_6W_6C—electrochemical measurements in 3.5 wt.% NaCl solution showed a corrosion potential of −0.188 V (Ag/AgCl), a polarization resistance of approximately $5×10^5$ $Ω·cm^2$, and a corrosion current density of 0.067 $μA·cm^{-2}$, corresponding to a very low corrosion rate of $6x10^{-4}$ mm·year-1. The results demonstrated that the stable Cr_2O_3/CoO passive film and the fine carbide network played a crucial role in effectively restricting charge transfer and localized corrosion. Overall, laser cladding with Stellite 6 significantly improved the surface integrity and corrosion resistance of AISI 1045 steel, demonstrating its suitability for applications in chloride-containing and marine environments.

Keywords - Stellite 6, Laser cladding, Corrosion resistance, Passive film, Electrochemical behavior.

1. Introduction

Steel, an essential and indispensable material in modern life, plays an irreplaceable role in the marine, aerospace, and chemical industries. However, when steel is exposed to corrosive environments with high levels of humidity, pH, and temperature, it often experiences serious corrosion [1, 2]. Therefore, applying surface treatment and corrosion protection methods can effectively reduce corrosion rates. These days, a variety of advanced surface-forming and treatment technologies have been developed, including thermal spraying, Physical Vapor Deposition (PVD), Electroplating, and Laser Cladding [3-6]. Various types of surface coatings have been shown to enhance the corrosion resistance of carbon steels [7-10].

A wide range of inorganic and organic compounds [11], polymers [12-14], and nanomaterials [15] have been utilized as corrosion inhibitors or protective materials. Sacrificial anodes, which mainly contain Cr and Zn, can adversely affect human health and the environment. Polymer coatings are relatively thick, and the significant difference in thermal conductivity between the polymer coating and metallic substrate can accelerate coating

degradation under thermal stress [16]. Nanocomposite coatings are widely employed in applications requiring high wear resistance, corrosion resistance, and hardness in harsh environments. However, the protective coatings often exhibit high electrical resistivity and hygroscopicity, leading to limited corrosion protection.

The main challenge is to develop more efficient and cost-effective alternatives to carbon steel substrates that are of strategic and economic importance. Cobalt-based alloy coatings, such as Stellite, are characterized by outstanding wear and corrosion resistance [17-20]. Moreover, Stellite maintains the superior properties at high temperatures [21]. Its exceptional wear resistance primarily arises from the unique microstructural characteristics of the hard carbide phases dispersed within the Co–Cr matrix [22]. Stellite 6 is widely used in wear applications and corrosion resistance. The alloy is able to resist various forms of mechanical and chemical degradation, so it is widely utilized. Due to its characteristics, it is commonly employed as a protective coating for valve and pump components in the petrochemical, energy, and food-processing industries [23, 24].

Laser cladding technology emerged along with the development of laser processing and surface engineering techniques [25-27]. In the process, a high-energy laser beam is used to melt both the coating material and e the substrate's surface layer, followed by rapid solidification, a metallurgically bonded coating is formed. The technology can be effectively utilized to enhance the surface mechanical properties of new components and to restore and repair worn or damaged parts [28, 29].

According to the above analysis, the excellent wear and corrosion resistance of Stellite 6 was established. However, the corrosion protection mechanism of Stellite 6 coatings on AISI 1045 steel produced by laser cladding has not yet been quantitatively clarified at the electrochemical and microstructural levels. In this study, the microstructure of the Stellite 6 coating on AISI 1045 steel fabricated by laser cladding was examined, the formation mechanism of the protective layer was analyzed, and the quantitative corrosion resistance was evaluated using electrochemical measurements.

2. Materials and Methods
2.1. Theoretical Background

Stellite 6 forms and stabilizes a passive layer that protects the underlying metallic substrate. It is a cobalt-based (Co) alloy that has high hardness, excellent corrosion resistance, and high wear resistance, so it is widely used as a protective coating for surfaces in harsh service conditions. The typical chemical composition of Stellite 6 is listed in Table 1.

Table 1. Typical chemical composition of stellite 6 alloy

Element	Symbol	Content (wt.%)
Cobalt	Co	Bal
Chromium	Cr	28.6
Tungsten (Vonfram)	W	4.9
Carbon	C	1.3
Nickel	Ni	2.2
Iron	Fe	1.9
Silicon	Si	1.1
Manganese	Mn	0.3
Molybdenum	Mo	$0.1 \leq$

The Stellite 6 coating, primarily composed of Cobalt (Co), Chromium (Cr), Tungsten (W), and Carbon (C), provides effective protection for metallic substrates against corrosive attacks, particularly in acidic, alkaline, and high-temperature environments. The corrosion resistance mechanism of Stellite 6 consists of complex physical and chemical processes. One of the main protective mechanisms is the formation of a thin Chromium Oxide (Cr_2O_3) layer on the coating surface when exposed to oxygen in air or a corrosive environment. The oxide layer helps prevent the direct interaction between the metal and corrosive agents. The chemical reaction for the formation of the Cr_2O_3 oxide film is as follows:

$$4Cr + 3O_2 \rightarrow 2Cr_2O_3$$
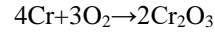
The partial-current Tafel equation for the anodic polarization branch is given by [30, 31]:

$$i_a = i_{corr} 10^{\eta/\beta_a}, i_c = i_{corr} 10^{-\eta/\beta_c}$$

Where β_a, β_c - the Tafel slopes for the anodic and cathodic branches; η - the overpotential, defined as: $\eta = E - E_{corr}$

Where E - the electrode potential (V); E_{corr} - the corrosion potential, representing the potential at which the anodic and cathodic currents are equal.

The polarization resistance at the corrosion potential E_{corr} Is given by:

$$R_p = \left(\frac{dE}{di}\right)_{\eta \to 0} = \frac{1}{\left(\frac{di}{dE}\right)_{\eta \to 0}} = \frac{1}{\left(\frac{di}{d\eta}\right)_{\eta \to 0}} \quad (1)$$

By differentiating at $\eta \to 0$, we obtain:

$$\left.\frac{di}{d\eta}\right|_{\eta \to 0} = i_{corr} \ln 10 \left(\frac{1}{\beta_a} + \frac{1}{\beta_c}\right)$$

Therefore:

$$R_p = \frac{\beta_a \beta_c}{2.303 i_{corr}(\beta_a + \beta_c)} \quad (2)$$

Let:

$$B = \frac{\beta_a \beta_c}{2.303(\beta_a + \beta_c)}$$

Then:

$$i_{corr} = \frac{B}{R_p} \quad (3)$$

The Corrosion Rate (CR) was calculated using Faraday's law [32-34]:

$$CR = \frac{i_{corr} \cdot M}{n.F.\rho} \quad (cm/s) \quad (4)$$

Where i_{corr} - the corrosion current density (A/cm^2); M - the molar mass *(g/mol)*; n – the number of electrons exchanged; F = 96485 *C/mol*; p - the density (g/cm^3)

According to ASTM G102 [35], Equation (4) can be rewritten as:

$$CR = 3.27x10^{-3} \frac{i_{corr} \cdot EW}{\rho} \ (mm/yr) \quad (5)$$

Where $i_{corr}(\mu A/cm^2)$; EW – Equivalent Weight (g/eq)

For alloy: $\frac{1}{EW} = \sum_i \frac{f_i.n_i}{A_i}$

Where: f_i - the mass fraction of an element; n_i - the valence in dissolution, A_i - the atomic weight of element *i*.

From the above relations, a smaller corrosion current density i_{corri} leads to a lower Corrosion Rate (*CR*) [23, 36].

The Cr_2O_3 oxide layer is highly stable and forms a passive film that protects the surface against chemical corrosion and attack by ions in corrosive environments. With a stable Cr_2O_3 passive film, the appropriate EIS equivalent circuit is as follows:

$$R_s - (R_f \| CPE_f) - (R_{ct} \| CPE_{dl})$$

Here: R_s - solution resistance $\Omega \cdot cm^2$; R_f - film resistance of the Cr_2O_3 passive layer ($\Omega \cdot cm^2$); R_{ct}- charge transfer resistance; CPE_f - constant phase element of the film; CPE_{dl} - constant phase element of the electric double layer.

The total polarization resistance is:

$$R_p = R_f + R_{ct} \tag{6}$$

Accordingly, the corrosion current density and corrosion rate in the presence of the Cr_2O_3 passive film are as follows:

$$i_{corr} = \frac{B}{R_f + R_{ct}} \tag{7}$$

$$CR = 3.27x10^{-3} \frac{B.EW}{(R_f + R_{ct})\rho} \ (mm/yr \tag{8}$$

In Stellite 6, the formation of carbide phases (Cr_7C_3 and Co_6W_6C) enhances the resistance to mechanical wear and corrosion. The carbide formation reactions proceed as follows:

$$7Cr+3C \rightarrow \rightarrow Cr_7C_3$$

$$Co+W+C \rightarrow Co_6W_6C$$
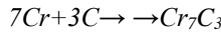
These carbides create hard structural constituents capable of resisting wear-induced damage, thereby protecting the coating against mechanical and corrosive actions. The surface energy delivered by a laser beam with a near-Gaussian distribution instantaneously melts the Stellite 6 powder (Co–Cr–W–C) while thinly remelting the AISI 1045 steel substrate to form a metallurgical bond [37-40]. Laser cladding generates a thermal field with a high cooling rate, leading to grain refinement and a dense coating with reduced porosity, which suppresses typical pitting initiation sites in chloride-containing media. Consequently, the fine and continuous microstructure stabilizes the passive film and improves the electrochemical response: a more continuous passive layer and slower charge transfer increase R_f and R_{ct}, which in turn decrease icorr and reduce CR in the NaCl environment.

2.2. Experimental Procedure

The substrate material used in the study was AISI 1045 medium-carbon steel with dimensions of 150 mm×60 mm×20 mm. The substrate surface was polished and cleaned with acetone before covering the laser cladding. The coating material was a spherical Stellite 6 alloy powder, a cobalt-based alloy with a particle size range of 50–150 μm, which was dried for 30 min before deposition.

The chemical compositions of the Stellite 6 powder and AISI 1045 steel substrate, as provided by the supplier, are listed in Table 1.The laser cladding process was performed using a Yb fiber laser system (Raycus RFL-C6000) equipped with a coaxial powder-feeding nozzle mounted on a three-axis CNC platform. The powder feeding system was controlled by a rotating disk feeder and transported to the laser head through a stream of argon gas to prevent oxidation during deposition. The process parameters of the laser cladding operation were programmed and precisely controlled using computer software. The laser cladding parameters are summarized in Table 2.

Table 2. The parameters of the laser cladding process

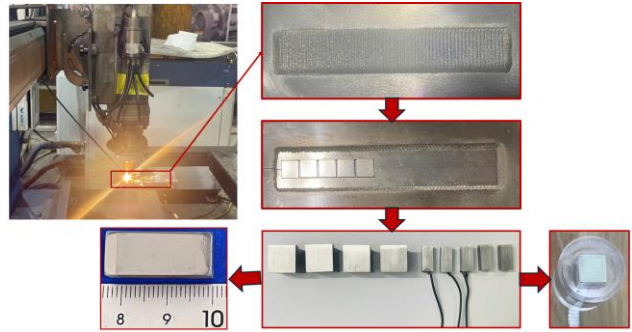| Parameters	Value
Laser power, kW	2000
Scanning speed, mm/min	800
Powder feeding rate, g/min	18
Powder feeding gas, l/min	7.2
Shielding gas, l/min	22
Laser spot size diameter, mm	33
Focus distance, mm	16
Overlapping ratio, %	50
Coating thickness, mm	2

Fig. 1 Coating and sample preparation

After cladding, the samples were cut by wire electrical discharge machining into specimens with dimensions of 10 mm×10 mm×20 mm, and then polished using SiC abrasive papers with grit sizes ranging from 1000 to 2000. The measurement surface was further polished with synthetic diamond paste and alumina powder and finally cleaned with pure ethanol. The polished and cleaned samples were dried in a vacuum oven for 30 min. The surfaces were etched to distinguish the material zones and grain morphology. The microstructure of the coating and interfacial region was observed using an Axiovert 40MAT optical microscope. For electrochemical corrosion testing, specimens of similar dimensions were prepared by wire cutting, followed by grinding and polishing to 0.05 μm, ultrasonic cleaning, and drying. An electrical wire was connected to the opposite side of the surface, while the remaining surfaces were covered with acrylic glue to prevent contact with the corrosive medium, leaving only the coating surface exposed with an area of 1.0 cm². The corrosion test was performed in a 3.5 wt—% NaCl solution simulating seawater conditions. Electrochemical corrosion resistance was measured using a Metrohm Stat-i 400s

instrument equipped with the DropView 8400 software. The samples were mounted in a three-electrode configuration consisting of the coated specimen as the working electrode, an Ag/AgCl reference electrode, and a Pt counter electrode, and maintained at a temperature of 25 ± 1 °C.
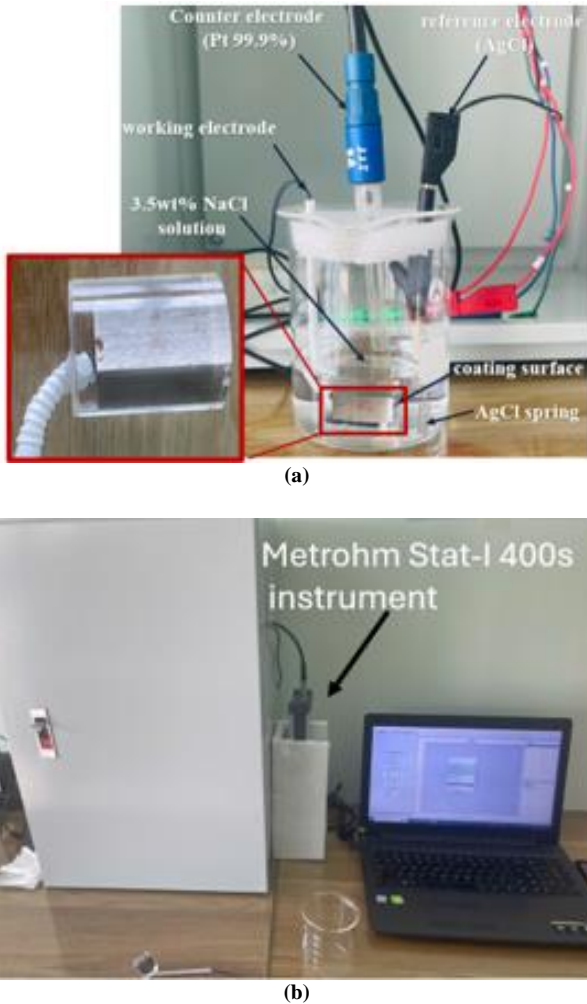

(a)

(b)

Fig. 2 Electrochemical corrosion measurement, (a) Electrochemical corrosion test setup, and (b) Electrochemical corrosion measurement process.

3. Results and Discussion

3.1. Microstructural Characteristics

Figure 3(a) shows the microstructure of the Stellite 6 coating on the AISI 1045 steel substrate. The coating exhibited a dense and uniform structure with a thin and continuous coating–substrate interface without observable defects, pores, or microcracks, indicating that a metallurgical bond was achieved in the conduction mode. The Heat-Affected Zone (HAZ) of the substrate was relatively narrow. The solidification morphology (Figure 3(b)) consisted of a Co-γ (FCC) matrix with columnar dendrites growing perpendicular to the interface and parallel to the heat transfer direction. The fine dendritic structure with small secondary arm spacing reflects the high cooling rate of the laser cladding process. The fine columnar morphology indicates high hardness and low defect density, providing a favorable surface for continuous formation of the Cr_2O_3 passive layer.
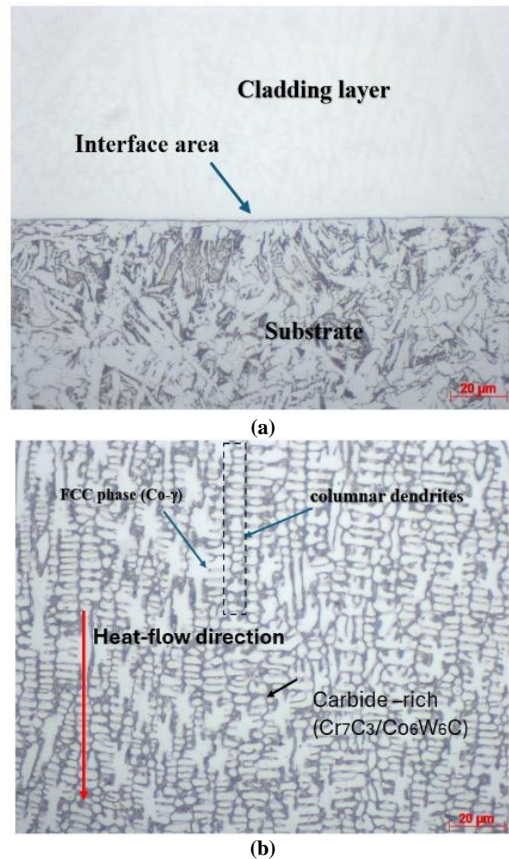

(a)

(b)

Fig. 3 Coating, (a) The microstructure at the interface zone of the coating/substrate, and (b) Microstructure of the coating at 500x magnification.

The grain size was measured using the line-intercept method, in which a series of test lines was superimposed on the micrograph and intersections with dendrite boundaries were systematically counted.

The grain size number was calculated automatically by the instrument software according to ASTM standards. The result showed a Grain Size Number Ø ≈ 12.6 (Figure 4), which indicated an ultrafine microstructure, which is characteristic of the rapid solidification typical of the laser cladding process. It refined microstructure significantly reduces microdefects, such as shrinkage pores and microcracks, which are potential initiation sites for pitting corrosion in a NaCl environment.
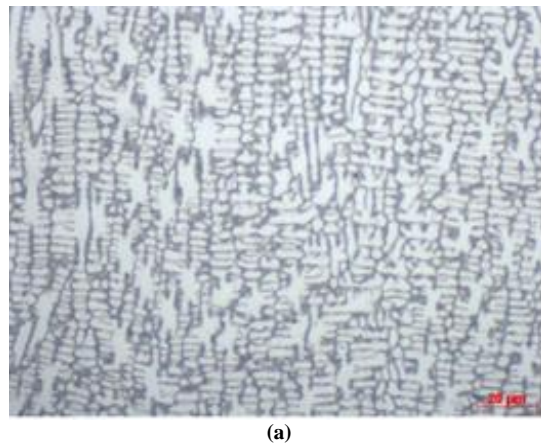

(a)

(b)
**Fig. 4 Grain size of the sample at the coating region,
(a) Original image, and (b) Image with annotations.**

3.2. Elemental Composition Analysis (EDS)

The EDS spectrum measured in the coating region (Spectrum 1, Figure 5) shows the following elemental composition: Co ≈ 51.7 wt.%, Cr ≈ 26.3 wt.%, W ≈ 3.84 wt.%, Mo ≈ 0.93 wt.%, with small amounts of Si (~1.44 wt.%) and Mn (~1.00 wt.%), and Fe only ~2.34 wt.%.The composition and ratio are consistent with Stellite 6 (Co–Cr–W–C steel). The low Fe content indicated a minimal degree of dilution from the AISI 1045 substrate that maintained a sufficient Cr concentration within the coating. The presence of W and Mo suggests the formation of Cr_7C_3 and Co_6W_6C carbides, which contribute to stabilizing the passive film. It aligns with the corrosion protection mechanism, in which a continuous Cr_2O_3/CoO passive layer enhances the Film Resistance (Rf), slows the dissolution kinetics, increases the Charge Transfer Resistance (Rct), and Consequently Reduces The Corrosion Current Density (icorr) and Corrosion Rate (CR) compared with the 1045 steel substrate.
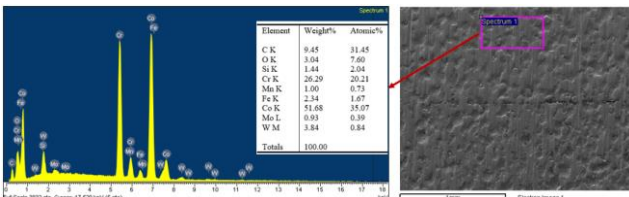

Fig. 5 SEM–EDS at the coating region of laser-clad stellite 6

Figure 6 shows the EDS spectrum at the interface between the Stellite 6 coating and 1045 steel substrate. EDS analysis revealed the simultaneous presence of coating elements (Co ≈ 24.9 wt.%, Cr ≈ 13.2 wt.%, W ≈ 1.65 wt.%, Mo ≈ 0.91 wt.%) and substrate elements (Fe ≈ 21.9 wt.%, Mn ≈ 1.06 wt.%, Si ≈ 1.11 wt.%). Compared with the coating region, the Fe content at the interface increased, whereas the Cr and Co contents decreased by approximately half, which corresponds to the localized mixing mechanism resulting from the partial melting of the substrate under the conduction mode. The coexistence of Co, Cr, W, and Fe confirmed the formation of a metallurgical bond with a compositional gradient, which reduced the stress concentration and minimized the risk of delamination.
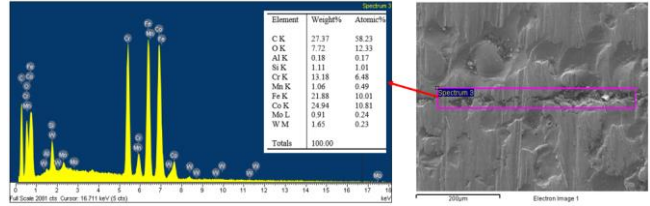

Fig. 6 SEM–EDS at the coating–substrate interface

The EDS spectrum of the substrate region (Spectrum 2) shows Fe ≈ 77.15 wt.%, C ≈ 12.63 wt.%, and O ≈ 6.70 wt.%. The Fe-rich composition confirms that the area corresponds to the substrate region located far from the melting interface, where the dilution from the coating is minimal. The result is consistent with the conduction-mode cladding process and narrow fusion zone observed in the cross-sectional image. Consequently, if the substrate is exposed during service, the film resistance R_f is lower, the charge transfer resistance R_{ct} decreases, and the corrosion current density i_{corr} increases significantly compared to the coated surface, leading to a more negative corrosion potential E_{corr} and higher icorr values. Additionally, when the Fe-rich substrate comes into contact with the electrolyte near the Co–Cr coating region, local galvanic microcells are formed, accelerating the localized dissolution of Fe along the exposed edges.
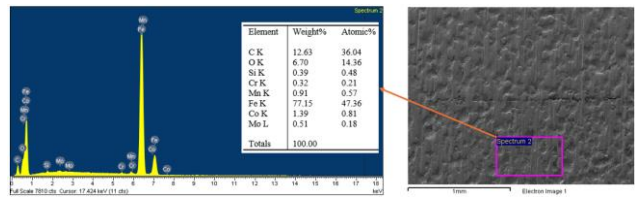

Fig. 7 SEM–EDS at the substrate region (aisi 1045) adjacent to the coating

3.3. Electrochemical Corrosion Resistance

Before the corrosion measurements, the working electrode was immersed in a 3.5 wt—% NaCl solution for 30 minutes to achieve a stable condition of the measured values. Subsequently, the open-circuit potential E_{ocp} was recorded as the basis for corrosion analysis, with the E_{ocp} stabilizing at approximately −0.185V.
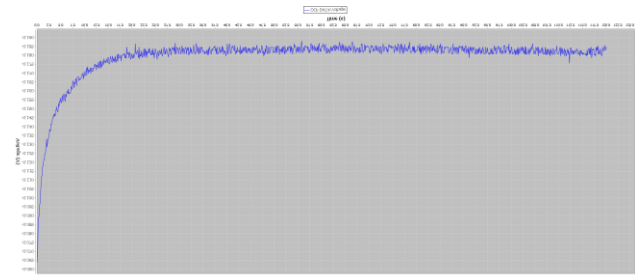

Fig. 8 Open circuit potential (Eocp)

Figure 9 presents the potentiodynamic polarization curve of the Stellite 6 coating, showing two distinct Tafel regions around the corrosion potential. Potentiodynamic polarization tests were conducted in a 3.5 wt.% NaCl solution using an Ag/AgCl reference electrode and a working electrode area of 1 cm², with a potential scan

range of -0.288 to $+0.076$ V, a step size of 1 mV, and a scan rate of 5 mV·s^{-1}. Two distinct Tafel slopes were observed near the corrosion potential. The obtained parameters were $E_{corr} = -0.1897V\ (\frac{Ag}{AgCl})$, $\beta_a = 0.12354V\,dec^{-1}$, $\beta_c = 0.42790V\,dec^{-1}$, and polarization resistance $Rp = 4.6930 \times 10^5\ \Omega$ (for a 1 cm² working area).

From the Tafel slopes (β_a and β_c) and the Stern–Geary constant, B, the value of 0.041597 V was determined. Using Equation (3), the corrosion current was calculated as:

$$i_{corr} = \frac{B}{R_p} = \frac{0.041597}{4.6930x10^5} = 0.08864\mu A$$

corresponding to a very low corrosion current density of $j_{corr} = 0.0887\ \mu Acm^{-2}$.

According to the ASTM G102 standard, the calculated corrosion rate was

$$CR = 1.99x10^{-3}mm\ yr^{-1}\ (0{,}07851\ mpy)$$

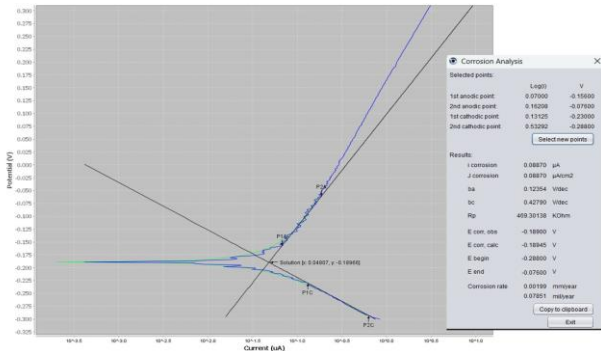**Fig. 9 Tafel polarization curve and corrosion analysis results of the stellite 6 alloy laser cladding sample**

The icorr value calculated using the Stern–Geary equation agreed well with the software results, confirming the reliability of the fitted Tafel region. The condition $\beta_c \gg \beta_a$ Indicates that the cathodic reaction (O$_2$/H$^+$ reduction) is more strongly polarized, consistent with the presence of a dense Cr$_2$O$_3$/CoO passive film limiting charge transfer. Within the scanning potential window of -0.288 to $+0.076$ V, no passive film breakdown was observed, demonstrating that the passive layer remained stable in the chloride environment. The very high Rp and extremely low CR values are consistent with the EIS spectra and correspond well with the coating microstructural characteristics—fine columnar dendrites, high Co–Cr content, low Fe dilution, and Cr-rich carbides - which collectively explain the increase in R_f and R_{ct}, leading to reduced icorr and CR.

Figure 10 shows the Bode plot of the Stellite 6 coating. The impedance modulus |Z| (blue points) decreased almost linearly on a log–log scale from 10^{-2} to 10^5 Hz. At very low frequencies, |Z| reaches approximately 5 × 10^5 Ω, whereas at high frequencies, it drops to approximately 10–15 Ω, with a phase angle near 0°, corresponding to the solution resistance Rs. The phase

angle curve (green points) shows a broad peak of approximately 80–90° in the mid-frequency range of several tens of hertz, indicating a dominant time constant associated with the passive film. From the Bode plot, the polarization resistance was estimated as $Rp \approx 5.0 \times 105$ Ω, and with the Stern–Geary constant B ≈ 0.0338 V, the corrosion current density was calculated as $i_{corr,EIS} = \frac{B}{R_p} = 0.068\mu A/cm^2$, which agrees well with the value obtained from the Tafel analysis. This confirms that the Cr$_2$O$_3$/CoO passive film was thin but compact, exhibiting slow anodic dissolution kinetics.

The results confirm that laser cladding with Stellite 6 is an effective method for significantly enhancing the surface performance of 1045 steel in terms of both mechanical properties and corrosion resistance.
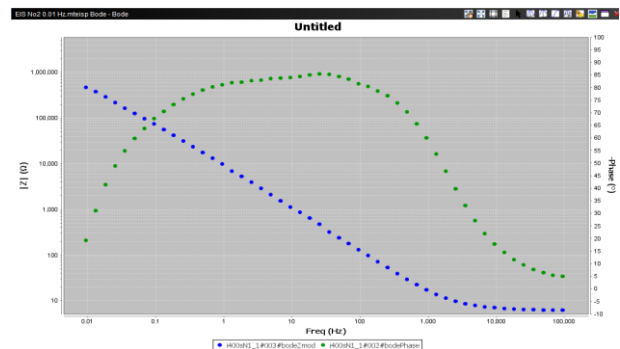

Fig. 10 Bode plot of the laser-clad stellite 6 coating at ecorr

4. Conclusion

The study demonstrated that the coaxial laser cladding of Stellite 6 on AISI 1045 steel resulted in a dense microstructure with fine columnar dendrites and a dispersed network of Cr$_7$C$_3$/Co$_6$W$_6$C carbides, along with minimal dilution. The metallurgical bonding formed under the conduction mode results in a narrow fusion zone, reduced defects, and improved chemical stability.In a 3.5 wt.% NaCl solution, the Tafel polarization results show *Ecorr≈− 0,188 V (Ag/AgCl), Rp≈5×105 Ω, Jcorr≈0,067 μA cm−2*, and a corrosion rate $CR \approx 6 \times 10^{-4}$ mm·year^{-1} (ASTM G102). The EIS results at *Ecorr* indicate |Z|$_{0.01}$ Hz ≈ 5 × 10^5 Ω and a broad phase angle peak (~85–90°). The equivalent circuit model $Rs−(Rf\|CPEf)−(Rct\|CPEdl)$ revealed high *Rf* and *Rct* values, consistent with the Tafel (Stern–Geary) analysis. The corrosion protection mechanism is attributed to the formation of a stable Cr$_2$O$_3$/CoO passive film on the Cr–Co-rich surface, combined with fine carbides that reinforce the structure and promote repassivation of the surface. A high coating density minimizes pitting initiation sites. Overall, the results confirm that the Stellite 6 coating is well-suited for components operating in chloride-containing environments.

Acknowledgments

References

[1] Ahmed Y. Musa et al., "On the Inhibition of Mild Steel Corrosion by 4-amino-5-phenyl-4H-1, 2, 4-trizole-3-thiol," *Corrosion Science*, vol. 52, no. 2, pp. 526-533, 2010. [CrossRef] [Google Scholar] [Publisher Link]

[2] Wei Chang et al., "Characterizing Corrosion Properties of Graphene Barrier Layers Deposited on Polycrystalline Metals," *Surface and Coatings Technology*, vol. 398, 2020. [CrossRef] [Google Scholar] [Publisher Link]

[3] Xiang Ding et al., "Corrosion Behavior of High-Pressure Cold-Sprayed Zn30Al Alloy Coating on Q235 Steel," *Coatings*, vol. 14, no. 11, pp. 1-14, 2024. [CrossRef] [Google Scholar] [Publisher Link]

[4] B. Riah et al., "Textured Hexagonal and Cubic Phases of AlN Films Deposited on Si (100) by DC Magnetron Sputtering and High Power Impulse Magnetron Sputtering," *Thin Solid Films*, vol. 655, pp. 34-40, 2018. [CrossRef] [Google Scholar] [Publisher Link]

[5] Jinliang Zhang et al., "A Review of Selective Laser Melting of Aluminum Alloys: Processing, Microstructure, Property and Developing Trends," *Journal of Materials Science & Technology*, vol. 35, no. 2, pp. 270-284, 2019. [CrossRef] [Google Scholar] [Publisher Link]

[6] Ping Zhu et al., "Effect of Nanoscale W Coating on Corrosion Behavior of Diamond/Aluminum Composites," *Nanomaterials*, vol. 13, no. 2, pp. 1-15, 2023. [CrossRef] [Google Scholar] [Publisher Link]

[7] Qiang Ma et al., "Fabricating Robust and Repairable Superhydrophobic Surface on Carbon Steel by Nanosecond Laser Texturing for Corrosion Protection," *Applied Surface Science*, vol. 455, pp. 748-757, 2018. [CrossRef] [Google Scholar] [Publisher Link]

[8] Ghulam Yasin et al., "Revealing the Erosion-Corrosion Performance of Sphere-Shaped Morphology of Nickel Matrix Nanocomposite Strengthened with Reduced Graphene Oxide Nanoplatelets," *Diamond and Related Materials*, vol. 104, 2020. [CrossRef] [Google Scholar] [Publisher Link]

[9] Madjid Sarvghad, Darwin Del Aguila, and Geoffrey Will, "Optimized Corrosion Performance of a Carbon Steel in Dilute Sulfuric Acid through Heat Treatment," *Applied Surface Science*, vol. 491, pp. 460-468, 2019. [CrossRef] [Google Scholar] [Publisher Link]

[10] Emad E. El-Katori, Yasser M. Al Angari, and Ashraf S. Abousalem, "Corrosion Mitigation of Carbon Steel by Spin Coating with Ag-TiO$_2$ Gel Films in Acidic Solution: Fabrication, Characterization, Electrochemical and Quantum Chemical Approaches," *Surface and Coatings Technology*, vol. 374, pp. 852-867, 2019. [CrossRef] [Google Scholar] [Publisher Link]

[11] F.X. Perrin, F. Ziarelli, and A. Dupuis, "Relation between the Corrosion Resistance and the Chemical Structure of Hybrid Sol-Gel Coatings with Interlinked Inorganic-Organic Network," *Progress in Organic Coatings*, vol. 141, 2020. [CrossRef] [Google Scholar] [Publisher Link]

[12] Chi-Hao Chang et al., "Novel Anticorrosion Coatings Prepared from Polyaniline/Graphene Composites," *Carbon*, vol. 50, no. 14, pp. 5044-5051, 2012. [CrossRef] [Google Scholar] [Publisher Link]

[13] Xuanyi Wang et al., "Recent Progress of Polymeric Corrosion Inhibitor: Structure and Application," *Materials*, vol. 16, no. 8, pp. 1-26, 2023. [CrossRef] [Google Scholar] [Publisher Link]

[14] Mehdi Honarvar Nazari, and Xianming Shi, *Polymer-Based Nanocomposite Coatings for Anticorrosion Applications*, Industrial Applications for Intelligent Polymers and Coatings, pp. 373-398, 2016. [CrossRef] [Google Scholar] [Publisher Link]

[15] Gan Cui et al., "New Method for CO$_2$ Corrosion Resistance Ni-W-Y$_2$O$_3$-ZrO$_2$ Nanocomposite Coatings," *Ceramics International*, vol. 45, no. 5, pp. 6163-6174, 2019. [CrossRef] [Google Scholar] [Publisher Link]

[16] Robert F. Cook, and Eric G. Liniger, "Stress-Corrosion Cracking of Low-Dielectric-Constant SpinOn-Glass Thin Films," *Journal of the Electrochemical Society*, vol. 146, pp. 4439-4448, 1999. [CrossRef] [Google Scholar] [Publisher Link]

[17] Raja Dharavathu, Kishora Shetty, and Gopinath Muvvala, "A Study on Laser Cladding of Stellite 6 by Conventional and High-Speed Laser Cladding Process," *Surface and Coatings Technology*, vol. 515, 2025. [CrossRef] [Google Scholar] [Publisher Link]

[18] Xu Liu et al., "Studies on High Power Laser Cladding Stellite 6 Alloy Coatings: Metallurgical Quality and Mechanical Performances," *Surface and Coatings Technology*, vol. 481, 2024. [CrossRef] [Google Scholar] [Publisher Link]

[19] Qifang Yu et al., "Comparative Investigation on the Microstructure and Corrosion Properties of Surfacing Cobalt Alloys by Various Methods," *Surface and Coatings Technology*, vol. 494, 2024. [CrossRef] [Google Scholar] [Publisher Link]

[20] C.R.C. Lima et al., "Wear and Corrosion Performance of Stellite 6® Coatings Applied by HVOF Spraying and GTAW Hotwire Cladding," *Journal of Materials Processing Technology*, vol. 284, 2020. [CrossRef] [Google Scholar] [Publisher Link]

[21] R. Ahmed, A. Fardan, and S. Davies, "Mapping the Mechanical Properties of Cobalt-Based Stellite Alloys Manufactured via Blending," *Advances in Materials and Processing Technologies*, vol. 10, no. 3, pp. 2531-2560, 2023. [CrossRef] [Google Scholar] [Publisher Link]

[22] G.N. Karimi et al., "The Role of Microstructural Development in the Hydrothermal Corrosion of Cast and HIPed Stellite 6 Analogues in Simulated PWR Conditions," *Corrosion Science*, vol. 159, 2019. [CrossRef] [Google Scholar] [Publisher Link]

[23] Irina Smolina, and Karol Kobiela, "Characterization of Wear and Corrosion Resistance of Stellite 6 Laser Surfaced Alloyed (LSA) with Rhenium," *Coatings*, vol. 11, no. 3, pp. 1-15, 2021. [CrossRef] [Google Scholar] [Publisher Link]

[24] Raghuvir Singh et al., "Laser Cladding of Stellite 6 on Stainless Steel to Enhance Solid Particle Erosion and Cavitation Resistance," *Surface and Coatings Technology*, vol. 251, pp. 87-97, 2014. [CrossRef] [Google Scholar] [Publisher Link]

[25] Bowen Chen et al., "Microstructure and Mechanical Properties of NiCoCrAlY Laser Cladding Coating after High-Current Pulsed Electron Beam Irradiation," *Philosophical Magazine Letters*, vol. 103, no. 1, pp. 1-12, 2023. [CrossRef] [Google Scholar] [Publisher Link]

[26] Zhijie Jing et al., "Residual Stress Release During Laser Cladding Process: A Review," *Journal of Laser Applications*, vol. 35, no. 3, 2023. [CrossRef] [Google Scholar] [Publisher Link]

[27] Lipeng Jiang et al., "Design and Characterization of a Novel $Cu_{2.3}Al_{1.3}Ni_{1.7}SnCr_{0.3}$ Multi-Principal Element Alloy Coating on Magnesium Alloy by Laser Cladding," *Journal of Materials Science & Technology*, vol. 152, pp. 220-236, 2023. [CrossRef] [Google Scholar] [Publisher Link]

[28] Jeng-Ywan Jeng, and Ming-Ching Lin, "Mold Fabrication and Modification Using Hybrid Processes of Selective Laser Cladding and Milling," *Journal of Materials Processing Technology*, vol. 110, no. 1, pp. 98-103, 2001. [CrossRef] [Google Scholar] [Publisher Link]

[29] Jiafu Pei et al., "Microstructure Evolution and Property of High Manganese Steel Coatings by Laser Shock Assisted Laser Wire Cladding," *Journal of Materials Processing Technology*, vol. 328, 2024. [CrossRef] [Google Scholar] [Publisher Link]

[30] Estelle Lebègue, "Electrochemical Methods: Fundamentals and Applications," 3rd ed., *Transition Metal Chemistry*, vol. 48, pp. 433-436, 2023. [CrossRef] [Google Scholar] [Publisher Link]

[31] E. Gileadi, and E. Kirowa-Eisner, "Some Observations Concerning the Tafel Equation and its Relevance to Charge Transfer in Corrosion," *Corrosion Science*, vol. 47, no. 12, pp. 3068-3085, 2005. [CrossRef] [Google Scholar] [Publisher Link]

[32] Dong-Ho Shin et al., "Evaluation of Commercial Corrosion Sensors for Real-Time Monitoring of Pipe Wall Thickness under Various Operational Conditions," *Sensors*, vol. 22, no. 19, pp. 1-29, 2022. [CrossRef] [Google Scholar] [Publisher Link]

[33] Carlos Alberto Montilla et al., "Corrosion Behavior of an AISI/SAE Steel Cut by Electropulsing," *Materials*, vol. 12, no. 22, pp. 1-15, 2019. [CrossRef] [Google Scholar] [Publisher Link]

[34] Peter Jurči et al., "Effect of Sub-Zero Treatments and Tempering on Corrosion Behaviour of Vanadis 6 Tool Steel," *Materials*, vol. 14, no. 13, pp. 1-24, 2021. [CrossRef] [Google Scholar] [Publisher Link]

[35] ASTM G102-23: Standard Practice for Calculation of Corrosion Rates and Related Information from Electrochemical Measurements, ASTM International, 2023. [Online]. Available: https://store.astm.org/g0102-23.html

[36] F. Rosalbino, and G. Scavino, "Corrosion Behaviour Assessment of Cast and HIPed Stellite 6 Alloy in a Chloride-Containing Environment," *Electrochimica Acta*, vol. 111, pp. 656-662, 2013. [CrossRef] [Google Scholar] [Publisher Link]

[37] Ana Vidergar, Andrej Jeromen, and Edvard Govekar, "Influence of the Laser-Beam Intensity Distribution on the Performance of Directed Energy Deposition of an Axially Fed Metal Powder," *Journal of Materials Processing Technology*, vol. 327, pp. 1-16, 2024. [CrossRef] [Google Scholar] [Publisher Link]

[38] Yuze Huang, Mir Behrad Khamesee, and Ehsan Toyserkani, "A Comprehensive Analytical Model for Laser Powder-Fed Additive Manufacturing," *Additive Manufacturing*, vol. 12, pp. 90-99, 2016. [CrossRef] [Google Scholar] [Publisher Link]

[39] Mehran Ghasempour-Mouziraji et al., "A Review Study On Metal Powder Materials and Processing Parameters in Laser Metal Deposition," *Optics & Laser Technology*, vol. 170, pp. 1-22, 2024. [CrossRef] [Google Scholar] [Publisher Link]

[40] Zhengtao Gan et al., "Modeling of Thermal Behavior and Mass Transport in Multi-Layer Laser Additive Manufacturing of Ni-based Alloy on Cast Iron," *International Journal of Heat and Mass Transfer*, vol. 111, pp. 709-722, 2017. [CrossRef] [Google Scholar] [Publisher Link]